A plasma discharge model of a microwave plasma diamond CVD reactor

Pushpa Mahalingam[1] and David S. Dandy
Department of Chemical Engineering
Colorado State University
Fort Collins, Colorado 80523

Abstract

A self-consistent electromagnetic field model and a fluid plasma model have been developed for a microwave plasma reactor used for diamond chemical vapor deposition. The coupled numerical models simulate the electromagnetic excitation of the hydrogen discharge and the hydrogen plasma discharge characteristics. The time-varying electric and magnetic fields inside the reactor, both inside and outside the plasma discharge region, are obtained by applying a finite-difference time-domain method to solve Maxwell's equations. The electromagnetic field interactions with the plasma discharge are described using electron and ion momentum transport equations. The plasma discharge characteristics are simulated using a fluid plasma model which solves the electron and ion continuity equations, electron energy balance equation, and the Poisson equation. Simulations have been performed to study the effect of input power and pressure on hydrogen discharge characteristics such as the electron temperature and plasma density.

Introduction

Microwave plasma assisted diamond chemical vapor deposition (CVD) is a commonly-used technique for diamond growth [1-5]. Such reactors have been extensively studied during the last several years in an effort to develop satisfactory plasma transport models that provide an estimation of species and temperature spatial distributions in the deposition chamber [6-15]. However, to date the studies have involved development of one-dimensional plasma discharge models [6, 12-14], in simple reactor geometries [7]. It is widely recognized that an understanding of the microwave excited plasma discharge characteristics and its sensitivity to process parameters such as the ambient pressure and input power are essential

---

[1] Present Address: Texas Instruments Inc.
13121 TI Blvd., MS 352, Dallas, TX 75243

to correctly determine the flow field, temperature, and concentrations of activated species at the substrate surface. In order to understand the behavior of the plasma inside a reactor, the coupled relationship between the multidimensional microwave fields, gas transport, and energy transport need to be investigated. To accurately explain these issues, a self-consistent two-dimensional numerical model is developed that simulates the electromagnetic fields as well as the excitation mechanism and characteristics of the plasma discharges used during diamond CVD in a microwave plasma reactor.

In this study, the microwave plasma is excited by coupling the microwave energy into the discharge by joule heating [16]. The electromagnetic field energy is imparted to the electron gas, where the energy is then transferred to ions and neutrals by elastic and inelastic collisions. The electromagnetic fields inside the reactor are determined by the finite-difference time-domain (FDTD) method [17]. The FDTD method is a non-traditional approach to numerical electromagnetics for engineering applications where analytic methods such as the frequency-domain integral equation approaches have dominated for almost three decades [18]. The FDTD method has been utilized in recent studies for the solution of three-dimensional scattering problems, lossy dielectric materials, resonant cavities, and electromagnetic fields inside a compact electron cyclotron resonance ion source [19-21]. The FDTD method has the advantage over analytical methods of ease of implementation for complicated geometries, because spatially varying dielectric parameters can be assigned using grid points. Moreover, most of the plasma numerical models may be easily coupled to the FDTD model because both are in the time domain.

The numerical model developed here for plasma discharge simulation is the fluid (continuum) plasma model, which solves for the moments of the Boltzmann equation, including the continuity equation, momentum transport equation, and energy transport equation. The electric fields causing plasma excitation inside the plasma discharge are governed by Poisson's equation. A self-consistent electromagnetic and plasma discharge solution is obtained by iteratively solving the coupled electromagnetic field and the fluid plasma models. The details of the coupling of the FDTD electromagnetic field model and the fluid plasma model are provided in the following sections.

A 6-inch inside diameter microwave plasma reactor loaded with a hydrogen discharge is simulated in this study. The hydrogen plasma was chosen because diamond film deposition processes consist of high percentages of hydrogen in the discharge [1, 2]. As shown by Koemtzopoulos et al. [7], adding small amounts of methane to a hydrogen discharge has only a minimal effect on the electron energy distribution function. The spatial electric field patterns, power absorption patterns, plasma density, electron energy, and plasma potential, are simulated and analyzed for different input conditions.

Background

Electromagnetic field model review

In this section, a review of the electromagnetic field model and the plasma discharge model is presented. The electromagnetic fields in a system can be obtained by solving the differential form of Maxwell's equations in either the time domain or the frequency domain. To solve the electromagnetic fields in the frequency domain, electromagnetic quantities such as the electric and magnetic fields are often assumed to be time-harmonic, that is, their time dependence can be described by a periodic sinusoid which is included in Maxwell's equations as a factor of the form $e^{j\omega t}$, where ω is the frequency of the imposed electromagnetic fields [22]. Then, the Maxwell equations are converted to vector Helmholtz equations, and the electric and magnetic fields are solved analytically in cylindrical coordinates (for a cylindrical cavity) in terms of a set of Bessel function-type solutions [22]. One major difficulty in applying the frequency domain electromagnetic field solutions is the geometry of the plasma discharge. If the load is geometrically complex, the number of boundary conditions needed for field solutions increases, leading to intractable computer solutions.

An alternative approach to determine the electromagnetic field inside the cavity is to directly solve the time-dependent Maxwell's equations by using a finite difference time-domain method. The FDTD technique was first proposed to examine interactions of electromagnetic waves with a perfectly conducting material [17]. In that model, the time-dependent Maxwell's equations in a rectangular coordinate system were expanded to a set of six scalar equations which were further discretized in both the time and space domain to obtain a set of finite difference equations. The numerical solutions of the FDTD model can achieve second order accuracy both in space and time by a staggered spatial mesh arrangement and by the leapfrog time marching method.

Review of plasma discharge models

Generally, for plasma-aided processing, there are two major approaches to simulate the transport behavior of discharges. One is the particle approach, which is carried out using a particle simulation technique that treats the plasma as a combination of particles (electrons, ions, neutrals) and calculates the trajectories of many particles in time to obtain the macroscopic quantities of the plasma [23-27]. This technique is particularly well suited for low pressure (mTorr), ECR, and non-equilibrium discharge simulation. However, its inherently time-consuming nature largely reduces its efficiency when implemented in computer programs. This is especially unattractive for simulation domains much larger than the particle mean free path or three-dimensional simulations.

The other approach is the continuum (or fluid) method, which treats the plasma as a fluid and solves the moment equations of the Boltzmann transport equation (BTE), including the continuity equation, momentum transport equation and energy transport equation of each plasma species [28-30]. The fluid models and the particle models are sometimes coupled as a hybrid fluid/particle model to provide self-consistent solutions [31]. However, fluid models may not be applied when the mean free path of particles (particularly electrons) are not the smallest characteristic length in the system, for non-equilibrium discharges, or large density (or energy) gradient regions. However, the fluid models have the advantage of being less computationally-intensive than the particle model. Therefore, in this study the microwave discharges are modeled based on fluid techniques since the pressure typically used during diamond microwave plasma CVD is in the 10-100 Torr range [1-5].

Model Formulation

The overall numerical model includes an electromagnetic model and a fluid plasma model that are described in the following sections. The coupling of these two models is also described. The schematic of the reactor and the problem domain used for the FDTD model and the fluid plasma model is shown in Fig. 1. The microwave plasma reactor modeled in this work is cylindrical and is azimuthally symmetrical; therefore, a two-dimensional (r and z directions as shown in Fig. 1) cylindrical coordinate system is adopted in the discretization of the governing equations of the FDTD and fluid plasma models.

FDTD electromagnetic model

The electromagnetic fields inside the microwave plasma reactor are obtained by solving the time-dependent Maxwell's equations, which are given by [32]

$$\nabla \times \mathbf{E} = -\mu \frac{\partial \mathbf{H}}{\partial t} \tag{1}$$

and

$$\nabla \times \mathbf{H} = \epsilon \frac{\partial \mathbf{E}}{\partial t} + \mathbf{J}, \tag{2}$$

where **E** and **H** are the electric and magnetic fields, respectively, μ is the permeability, ϵ is the permittivity, and **J** is the current density induced by the applied electromagnetic fields. The Maxwell Eqs. (1) and (2) are discretized in two-dimensional cylindrical coordinates with a centered difference approximation in the space domain. The Maxwell equations are to be solved to determine the power absorbed by the plasma discharge. The power dissipation density, $P_{abs}(\mathbf{r}, \mathrm{t})$, with a power absorbing load (such as a discharge) present is

$$P_{abs}(\mathbf{r}, t) = \mathbf{J}(\mathbf{r}, t) \cdot \mathbf{E}(\mathbf{r}, t). \tag{3}$$

The current density, **J**, which is induced by the microwave fields, may be computed as [33]

$$\mathbf{J} = \frac{e^2\, n_e\, \nu_{eff}}{\left[m_e(\nu_{eff}^2 + \omega^2)\right]} \mathbf{E} = \sigma \mathbf{E}, \tag{4}$$

where e is the electron charge, m_e is the electron mass, ν_{eff} is the effective electron frequency, n_e is the electron density, and σ is the conductivity of the plasma. The effective collision frequency for the electrons, which describes the momentum transfer due to electron-neutral (in this case, electron-H_2) elastic collisions, is relatively insensitive to the electron temperature, so it may be written as [29]

$$\nu_{eff} = 1.44 \times 10^{12} \times \frac{P_{\mathrm{r}}}{T_{\mathrm{n}}}, \tag{5}$$

where P_{r} is the reactor pressure (Torr) and T_{n} is the temperature (K) of the neutral species.

From the above equations (1)-(4), it may be seen that the current density, **J**, depends on spatially-dependent discharge characteristics such as electron density and the electric field. The electron density must be determined in a self-consistent manner using a fluid plasma model.

The boundary conditions for the electric fields used in the FDTD model are described below. The metallic reactor walls and the substrate are assumed to be perfect conductors, such that the normal electric field components can exist and tangential components of the electric fields vanish on these surfaces. This boundary condition implies that the electromagnetic waves propagating to the perfectly-conducting wall boundaries would be totally reflected and no field would penetrate through these boundaries. Therefore, the grids used for the FDTD model may be truncated at the wall boundaries because no fields can exist outside these boundaries. However, the input end of the reactor where the microwave energy is imparted to the reactor is an open boundary, i.e., the domain in which the field has to be computed is unbounded. The electromagnetic waves, either incident or reflected, do exist outside the boundary and the number of grids needed for simulation becomes unlimited in principle. Therefore, at this open boundary a truncation method, which also prevents any artificial reflection of the outgoing wave, must be used for limiting the domain in which the field is computed. The schematic of the grid structure used in the electromagnetic field model is illustrated in Fig. 2. The non-reflecting boundary condition applied in this model may be written as [20]

$$E_r^{n+1}(i,k_0) = E_r^n(i,k_0-1) + \frac{[\Delta t/(\epsilon\mu)^{1/2} - \Delta z]}{[\Delta t/(\epsilon\mu)^{1/2} + \Delta z]} \times [E_r^{n+1}(i,k_0-1) - E_r^n(i,k_0)] \qquad (6)$$

and

$$E_\phi^{n+1}(i,k_0) = E_\phi^n(i,k_0-1) + \frac{[\Delta t/(\epsilon\mu)^{1/2} - \Delta z]}{[\Delta t/(\epsilon\mu)^{1/2} + \Delta z]} \times [E_\phi^{n+1}(i,k_0-1) - E_\phi^n(i,k_0)] \qquad (7)$$

where i denotes the grid location in the r-direction and k_0 is the grid terminating point in the z-direction.

The electric fields on the source points at the top end of the reactor as shown in Fig. 2 are prescribed to be [19]

$$E_r^{n+1}(i, k_1) = E_r^n(i, k_1) + C\sin(2\pi\omega t), \tag{8}$$

where C is the amplitude of the electric field source, k_1 is the grid plane where the source is located, and ω is the excitation frequency (in this case, 2.45 GHz).

Fluid Plasma Model

The behavior of the charged particles in a weakly ionized gas can be described by the particle, momentum, and energy balance equations for electrons and ions, which are obtained from the moments of the Boltzmann equation. These equations are often combined with Poisson's equation to provide a self-consistent space charge field. At steady state, Poisson's equation is written as [34]

$$\nabla^2\psi = \frac{e}{\epsilon}(n_e - n_i) \tag{9}$$

where ψ is the potential ($\mathbf{E} = -\nabla\psi$). The electron and ion continuity equations are represented by

$$\nabla \cdot \mathbf{J}_e = n_e n_n k_{\text{ion}} - \alpha_r n_i n_e \tag{10}$$

and

$$\nabla \cdot \mathbf{J}_i = n_e n_n k_{\text{ion}} - \alpha_r n_i n_e \tag{11}$$

respectively. The momentum balance equations for electrons and ions are given by

$$\mathbf{J}_e = -n_e\mu_e\mathbf{E} - D_e\nabla n_e \tag{12}$$

and

$$\mathbf{J}_i = n_i\mu_i\mathbf{E} - D_i\nabla n_i \tag{13}$$

respectively [35]. The first and second terms on the right hand sides of Eqs. (12) and (13) represent particle drift due to the applied electric field and the diffusive term due to the particle concentration gradient. The electron energy balance equation is given by

$$\begin{aligned}\nabla \cdot \mathbf{q}_e = e\mathbf{J}_e \cdot \mathbf{E} - n_e n_n(\epsilon_{\text{ion}}k_{\text{ion}} + \epsilon_{\text{ext}}k_{ext} + \epsilon_{\text{dis}}k_{\text{dis}})\\ -2\frac{m_e}{m_n}\left(\frac{3}{2}k_B T_e - \frac{3}{2}k_B T_n\right)\nu_m n_e\\ -\frac{3}{2}k_B T_e \alpha_r n_i n_e\end{aligned} \tag{14}$$

with the total electron energy flux given by

$$\mathbf{q}_e = \frac{5}{2}k_B T_e \mathbf{J}_e - \left(\frac{5}{2}k_B D_e n_e\right)\nabla T_e. \tag{15}$$

The first term in Eq. (15) is the kinetic energy and the second term is the thermal energy. In the above equations, n_e and n_i are the electron and ion densities, respectively; $\mathbf{J}_e$ and $\mathbf{J}_i$ are the electron and ion fluxes, respectively; T_e is the electron temperature; and $\mathbf{q}_e$ is the electron energy flux. For the partially-ionized and partially-dissociated H_2 plasma discharge processes simulated in this study, the major particle interactions are electron-H_2 gas inelastic collisions, electron-H_2 gas elastic collisions and electron-hydrogen ion recombination. The electron-H_2 inelastic collisions include H_2 gas ionization, excitation and dissociation processes. The rate coefficients for these collision processes are expressed using an Arrhenius relationship [35] as

$k_j = A_j \exp(-\epsilon_j / k_B T_e)$, where k_j is the inelastic rate constant and $j = ion$, ext, and dis, for the three processes of ionization, excitation, and dissociation. The threshold energy for each collision process is ϵ_j and A_j is the pre-exponential factor. The types of inelastic collisions in a H_2 discharge and their corresponding rate parameters are summarized in Table I. The reactions that are used here have been used previously to simulate a H_2 discharge [8, 34]. In Eqs. (10), (11), and (14), α_r is the recombination rate constant. The elastic losses are represented by the electron-neutral momentum transfer frequency, ν_m, which is assumed to be equal to the effective electron-neutral momentum transfer frequency (ν_{eff}), and m_n is the neutral species mass. The quantities $D_{e,i}$ and $\mu_{e,i}$ are the electron and ion diffusivities and mobilities, respectively.

The boundaries for the fluid plasma simulation are the substrate and the edge of the plasma volume. In this work, a set of experimentally-determined empirical equations developed by King [36] is used to determine the neutral temperature and plasma volume based on the pressure and the input microwave power. The empirical equations were formulated based on statistically-designed experimental data obtained by discharge diagnostics in a parameter space including microwave power and reactor pressure. The empirical equations used for the translational temperature of H_2 gas and the discharge volume are [36]

$$T_n = 226.6 + 374.3 P_{abs} + 16.5 P_r \pm 94.2 \tag{16}$$

and

$$V = 449.7 + 116.2 P_{abs} - 18.1 P_r + 57.1 P_{abs}^2 + 0.25 P_r^2 - 5.4 P_r P_{abs} \pm 15.4, \tag{17}$$

where the units for T_n, P_{abs}, and P_r are K, kW, and Torr respectively.

The boundary conditions for the fluid plasma model at the substrate and the edge of the plasma volume are

$$\begin{aligned} n_e = n_i &= 0, \\ T_e &= T_n, \\ \psi &= 0, \end{aligned} \tag{18}$$

and at the centerline $r = 0$,

$$\frac{\partial n_e}{\partial r} = \frac{\partial n_i}{\partial r} = \frac{\partial T_e}{\partial r} = \frac{\partial \psi}{\partial r} = 0. \tag{19}$$

Inside the plasma discharge volume region, the translational temperature given by Eq. (16) is equal to the neutral temperature [8].

Solution Method

Finite difference techniques are used to discretize the cylindrical coordinates form of Eqns. (9)–(15). Newton's method is used to solve the nonlinear, discretized equations, to obtain the electron temperature (T_e), electron density (n_e), ion density (n_i), and plasma potential (ψ). Note that the heating term, $e\mathbf{J}_e \cdot \mathbf{E}$ in Eq. (14), represents the microwave power absorbed by the plasma, which is determined from the FDTD electromagnetic field model. First, the electromagnetic fields are computed using the FDTD model with an assumed electron density distribution. The power absorbed by the plasma (P_{abs}) is then obtained from the FDTD model. The time domain used for the FDTD model is twenty microwave cycles because the total stored electromagnetic energy in the plasma reaches a steady state at this time. A steady state is reached because the input power from the source points equals the power absorbed by the plasma. Then, the approximate solutions for the electron (n_e) and ion densities (n_i), along with the P_{abs} field are input to the electron energy balance, Eq. (14), to determine the electron temperature (T_e). Next, the calculated electron temperature is input to the coupled Poisson Eq. (9), electron continuity Eq. (10), and ion continuity Eq. (11) equations, which are solved using Newton's method. From these equations, the unknowns computed at each grid point are the electron and ion densities (n_e, n_i), and plasma potential (ψ). The electron and ion fluxes are then determined from Eqs. (12) and (13) using the known electron and ion densities and the plasma potential. The calculated electron and ion densities and plasma potential are fed back to the electron energy balance equation. The converged discharge characteristics information is then transferred back to the FDTD model to modify the plasma conductivity and calculate a new power absorption. The final stable solution of electron density and temperature is achieved by iteratively solving the continuity, Poisson, electron energy balance and Maxwell equations.

Results and Discussion

Eight simulations were performed to examine the effects of power absorption by the plasma and reactor pressure on the plasma discharge characteristics. The input conditions for microwave power (400, 600, and 900 W) and pressure (15, 25, and 40 Torr) used in this study are the operating conditions used in our reactor to grow diamond films. The results are categorized into two areas based on the variation of absorbed power and system pressure in different runs. In each run, the plasma volume is computed using Eq. (17) and the substrate temperature is fixed at 1200 K. In this study, it is assumed that 100% of the microwave power coupled into the reactor is absorbed by the plasma.

Effect of Power Absorption

Four runs—I, II, III, and IV—were performed at the same reactor pressure (15 Torr), but for different absorbed power by the plasma, 30, 400, 600, and 900 W, respectively. Run parameters for each simulation are given in Table II.

The electric field and power absorption patterns are compared for the lowest (30 W, Run I) and highest (900 W, Run IV) power absorption by the plasma at a constant reactor pressure of 15 Torr. The simulation results for the electric field distribution in the entire reactor are shown in Figs. 3(a), and 3(b) for the radial component E_r and axial component E_z of the 30 W (Run I) case; and Figs. 4(a) and 4(b) correspond to the E_r and E_z field components of Run IV, 900 W. The effect of the electric field caused by the presence of the discharge may be observed in Figs. 5(a), 5(b), 6(a), and 6(b). The plasma discharge reduces the amplitude of the electric field in the plasma discharge region for runs I (30 W) and IV (900 W), since electromagnetic power is absorbed in the discharge region. The electric field patterns, i.e., E_r and E_z inside the plasma discharge region are shown in Figs. 5(a) and 5(b) for Run I (30 W) and 6(a) and 6(b) for Run IV (900 W) respectively. It may be seen that the E_z and the E_r fields do not simply decay into the discharge but are concentrated close to the plasma discharge center in the plasma simulation region. This behavior arises because the discharge has a finite size and the plasma density is not uniform. Therefore, the electric field propagates into the plasma simulation region and is concentrated within the region close to the center axis of the reactor without being blocked by the discharge. Figs. 7(a) and 7(b) illustrate the power absorption pattern for runs I (30 W) and IV (900 W) respectively. Fig. 7(a) indicates that the microwave power absorbed by the plasma is distributed fairly uniformly in the plasma region compared to Fig. 7(b) where most of the microwave power is absorbed primarily at the plasma boundaries, and not throughout the entire plasma volume.

The predicted electron temperatures are shown in Figs. 8(a) and 8(b) for Runs I and IV. The electron temperature is fairly uniform for Run I (30 W), as shown in Fig. 8(a) although the electron temperature is highest at the plasma boundaries for Run IV (900 W) as illustrated in Figs. 8(b). The corresponding results for electron density are shown in Figs. 9(a) and 9(b). The plasma density is high at the center of the discharge and at some points in the plasma boundary for Run I (30 W), as shown in Fig. 9(a); however, the plasma density is concentrated more at the plasma boundaries for Run IV (900 W) as shown in Fig. 9(b). The spatial variation of dissociation of H_2 is shown in Fig. 10 for Run II (400 W) and indicates that the dissociation rate is higher at the plasma boundaries due to the electron temperature and electron density being higher at that region.

The average electron temperature and maximum electron temperature in the plasma region are plotted versus power for different pressures in Figs. 11(a) and 11(b) to compare the effect of absorbed plasma power on electron temperature. Similarly, the average plasma density and maximum electron density in the plasma region are plotted versus power for different pressures in Figs. 12(a) and 12(b). The electron temperature increases with higher absorbed power (refer to Figs. 11(a) and 11(b)) because the measured neutral gas temperature increases with microwave power, as indicated by Eq. (16). The higher neutral gas temperature leads to a lower neutral density and, hence, to a reduced electron-neutral collision rate (which is an electron energy loss mechanism) at a given electron temperature. The plasma density increases with an increase in the absorbed microwave power at a given reactor pressure (see Figs. 12(a) and 12(b)) because the electron temperature increases with power. The higher electron temperature leads to a higher ionization rate, producing more electrons. It should be noted that the recombination rate of the electrons remains unaffected by the electron temperature (see Table I). The increase in the predicted average electron temperature with absorbed power agrees with published results [8].

The absorbed microwave power and the plasma density are concentrated at the plasma boundaries and not throughout the entire plasma volume at a higher absorbed power (greater than 30 W) (see Figs. 7(b) and 9(b)) because at higher absorbed power, the plasma density increases. The increase in plasma density leads to an increase in the plasma conductivity (see Eq. 4), which reduces the magnitude of the electric field exponentially with penetration into the plasma discharge region [37, 38] as the microwave skin depth decreases. The microwave skin depth (δ) is defined as the distance from the conductor surface (in this case, the plasma discharge surface) at which the magnitude of the electric fields have decreased to $1/\ell n^{-1}(1)$ (approximately 37%) of their values at the conductor surface. The microwave skin depth is $\delta = c/\omega_p$, where c is the speed of light and ω_p is the plasma frequency, given by $\omega_p = (n_e q^2/m_e \epsilon)^{1/2}$. The concentration of electric fields at the plasma boundaries at higher absorbed power leads to a concentration of absorbed microwave power and plasma density in that region. Such a phenomenon for the absorption of power at the plasma edges at high plasma density has been predicted by Tan and Grotjohn [39] and is also discussed in detail in the literature [37, 38]. Gicquel [40] reported an upper bound of 10^{18} m^{-3} for the plasma density above which the microwave energy would not be able to penetrate the plasma efficiently.

In the present study, a plasma density of 10^{18} m^{-3} is attained for absorbed plasma power greater than 30 W at 15 Torr pressure. This agrees with the experimental and modeling results reported by Kelkar et al. [41] in an argon plasma in a similar microwave reactor. Kelkar et al. [41] report an electron density of 10^{18} m^{-3} for an absorbed plasma power of 16.5 W at 5 Torr pressure. Interestingly, Kelkar et al. indicate that only 2%-5% (10-35 W) of the input power (680 W) coupled into their reactor is deposited in the plasma. It is speculated that the power coupling efficiency in the reactor system used in this study could be less than 100%, thereby in effect depositing less power in the plasma than is input into the reactor (i.e., 400 W, 600 W, and 900 W). Work is underway to measure the electric fields to determine the power absorbed in the plasma. In another similar study of a low pressure (10-100 mTorr) rf argon discharge, Kortshagen et al. [42] found that their numerically predicted electron number density exceeded those measured experimentally by around a factor of 4.

It is indicated that their assumption of 100% power absorption by the plasma may be the reason. Mak and Asmussen [43] also found that the Langmuir probe measurements of the electron number density in an argon plasma 3 cm downstream of the bulk plasma were a factor of 2-4 lower than those predicted from their simple global reactor model (for an input power of 277 W, 1-7 mTorr). It was argued that electron recombination between the bulk plasma and the downstream probe location would account for some of this discrepancy although it is suspected that the remaining discrepancy may be a result of a power coupling efficiency less than 100%.

Effect of Pressure

Three runs—II, V, VI were performed at the same absorbed microwave power (400 W) but at reactor pressures of 15, 25, and 40 Torr; runs IV, VII, and VIII were performed at the same absorbed microwave power of 900 W at pressures of 15, 25, and 40 Torr. The predicted average and maximum electron temperatures in the plasma are shown in Figs. 11(a) and 11(b). The electron temperature drops with increase in pressure because neutral density increases with pressure, as does the collision frequency between electrons and neutrals. Therefore, electrons more easily transfer their energy to neutral particles and reduce their kinetic energy. The simulation results of plasma density are shown in Figs. 12(a) and 12(b) for all the runs performed in this study. The average plasma density increases with increasing pressure since the neutral density increases linearly with increase in pressure leading to an increase in ionization rate producing more electrons and ions. However, the maximum predicted plasma density at pressures of 25 and 40 Torr are similar because the decrease in the ionization rate due to lower electron temperature at higher pressure is offset by the increase in ionization rate due to the higher neutral density at higher pressures. The predicted variation of average electron temperature and plasma density with pressure agree well with published experimental [44] and plasma modeling [45] studies although these studies were carried out at very low pressures (1-7 mTorr).

Summary

A self-consistent electromagnetic field model and a fluid plasma model is presented for a microwave plasma reactor operating under conditions characteristic of diamond chemical vapor deposition. The electromagnetic field model solved by the FDTD method is coupled to a fluid plasma model. The fluid plasma model is solved by the Newton-Raphson method. A microwave plasma reactor loaded with a H_2 discharge is simulated using this numerical model. The input parameters for the microwave plasma reactor simulation include the reactor pressure and absorbed microwave power. It is assumed in this study that 100% of the microwave power input into the reactor is absorbed by the plasma. The electromagnetic behavior of the discharge, including the electric field distributions and power absorption patterns, were studied for different input conditions. The characteristics of the plasma discharge (the electron temperature, plasma density, and ionization rate of H_2) were predicted for different input conditions.

It is found that, for constant absorbed microwave power, the electron temperature decreases with an increase in pressure, while the plasma density increases. At constant pressure it is found that both the electron temperature and plasma density increase with absorbed microwave power. At higher absorbed microwave power for constant reactor pressure, the electric fields, absorbed power, and plasma density are concentrated at the plasma boundaries instead of being distributed throughout the entire plasma volume because the microwave skin depth decreases with increasing microwave power. In this study, the plasma density and absorbed power are concentrated at the plasma boundaries for an absorbed plasma power greater than only 30 W at a reactor pressure of 15 Torr. It is therefore speculated that less than 100% of the power coupled into the reactor is deposited in the plasma. Work is in progress to conduct probe measurements of the electric field in our reactor to determine the power absorbed by the plasma.

Future studies would involve coupling the plasma model with a hydrodynamic model to simulate the flow, temperature, and concentration of hydrocarbon species in the microwave plasma diamond CVD reactor. Towards this end, the predicted electron elastic energy loss will be coupled to the energy equation in the hydrodynamic model to compute the increase in temperature of the gas due to momentum transfer between the electrons and the gas. The plasma density and electron temperature predicted by the plasma model will be used to compute the gas-phase reaction rates of electron-neutral and electron-ion reactions which affect the concentration and gas-to-substrate flux of various hydrocarbon ions and radicals (such as H, CH_3, etc.) responsible for diamond growth. The flux of the reactive species will be utilized in a microscopic scale Monte Carlo model to simulate diamond film growth and develop an understanding between the process-microstructure-property relationship during diamond CVD.

References

1. K. E. Spear, and M. Frenklach, Synthetic Diamond: Emerging CVD Science and Technology, eds. K. E. Spear, and J. P. Dismukes (John Wiley & Sons, Inc., 1994).
2. H. Liu and D. S. Dandy, Diamond Chemical Vapor Deposition: Nucleation and Early Growth Stages (Noyes Publications, Park Ridge, New Jersey, 1995).
3. D. M. Bhusari, J. R. Yang, and L. C. Chen, Solid State Comm.; an international

journal **107**, 301 (1998).

4. Y.-H. Chen, C.-T. Hu, and I.-N Lin, Appl. Surf. Sci. **113/114**, 231 (1997).
5. M. A. Khan, M. S. Haque, and A. P. Malshe, Thin Solid Films **332**, 93 (1998).
6. E. Hyman, K. Tsang, and A. Drobot, J. Vacuum Sci. Technol. A **12**, 1474 (1994).
7. C. R. Koemtzopoulos, D. J. Economou, and R. Pollard, Diam. Rel. Mater. **2**, 25 (1993).
8. W. Tan and T. A. Grotjohn, Diam. Rel. Mater. **4**, 1145 (1995).
9. E. Hyman, K. Tsang, I. Lottati, A. Drobot, B. Lane, R. Post, and H. Sawin, Surf. Coatings Technol. **49**, 387 (1991).
10. Y. A. Mankelevich, A. T. Rakhimov, N. V. Suetin, S. V. Kostiuk, Diam. Related Mater. **5**, 964 (1996).
11. Y. A. Mankelevich, A. T. Rakhimov, N. V. Suetin, Diam. Related Mater. **5**, 888 (1996).
12. M. Capitelli, G. Colonna, K. Hassouni, and A. Gicquel, Plasma Chem. Plasma Proc. **16**, 153 (1994).
13. K. Hassouni, S. Farhat, C. D. Scott, and A. Gicquel, J. de Physique III **6**, 1229 (1996).
14. K. Hassouni, O. Leroy, S. Farhat, and A. Gicquel, Plasma Chem. Plasma Proc. **18**, 325 (1998).
15. M. Funer, C. Wild, P. Koidl, Surf. Coatings Technol. **74-75**, 221 (1995).
16. J. Asmussen, J. Vac. Sci. Technol. A **7**, 883 (1989).
17. K. S. Yee, IEEE Trans. Antennas Propagat. **14**, 302 (1966).

18. A. Taflove and K. R. Umashankar, Electromagnetics **10**, 105 (1990).

19. A. Taflove and M. E. Brodwin, IEEE Trans. Microwave Theory Tech. **23**, 623 (1975).

20. G. Mur, IEEE Trans. Electromagn. Compat. **23**, 377 (1981).

21. T. A. Grotjohn, W. Tan, V. Gopinath, A. K. Srivatsava, and J. Asmussen, Rev. Sci. Instrum. **65**, 1312 (1994).

22. R. F. Harrington, Time-Harmonic Electromagnetic Fields (McGraw-Hill, 1961).

23. M. J. Kushner, J. Appl. Phys. **54**, 4958 (1983).

24. B. E. Thompson and H. Sawin, J. Appl. Phys. **63**, 2241 (1988).

25. J. I. Ulacia and J. P. McVittie, J. Appl. Phys. **65**, 1484 (1989).

26. G. R. Govinda Raja and M. S. Dincer, IEEE Trans. Plasma Sci. **18**, 819 (1990).

27. T. E. Sheridan, M. J. Goeckner, and J. Goree, Vac. Sci. Technol. A **8**, 30 (1990).

28. D. B. Graves and K. F. Jensen, IEEE Trans. Plasma Sci. **14**, 78 (1986).

29. D. B. Graves, J. Appl. Phys. **62**, 88 (1987).

30. J. P. Boeuf, Phys. Rev. A **36**, 2782 (1987).

31. Y. Weng and M. J. Kushner, J. Appl. Phys. **72**, 33 (1992).

32. A. Taflove, Computational Electrodynamics: A Finite-Difference Time-Domain Method (Artech House, Boston, 1995).

33. B. E. Cherrington, Gaseous Electronics and Gas Lasers (Pergamon, New York, 1979).

34. M. Surendra, D. B. Graves, and L. S. Plano, J. Appl. Phys. **71**, 5189 (1992).

35. J. D. P. Passchier and W. J. Goeheer, J. Appl. Phys. **74**, 3744 (1993).

36. G. King, Ph.D. Dissertation (Michigan State University, 1994).

37. S. Ramo, J. R. Whinnery, and T. Van Duzer, Fields and Waves in Communication Electronics (Wiley, New York, 1984).

38. Handbook of Plasma Processing Technology (Noyes Publications, Park Ridge, New Jersey, 1990), Ch. 3.

39. W. Tan and T. A. Grotjohn, J. Vac. Sci. Technol. A **12**, 1216 (1994).

40. A. Gicquel, in Handbbok of Industrial Diamonds and Diamond Films edited by M. Prelas, G. Popovici, and L. K. Bigelow (Marcel Dekker, New York, 1997), Ch. 13, pp. 590.

41. U. M. Kelkar, M. H. Gordon, L. A. Roe, and Y. Li, J. Vac. Sci. Technol. A **17**, 125 (1999).

42. U. Kortshagen, I. Puropski, and L. D. Tsendin, Phys. Rev. E **51**, 6063 (1995).

43. P. Mak and J. Asmussen, J. Vac. Sci. Technol. A **15**, 154 (1997).

44. S. M. Gorbatkin, L. A. Berry, and J. B. Roberto, J. Vac. Sci. Technol. A **8**, 2893 (1990).

45. M. Meyyappan and T. R. Govindan, J. Appl. Phys. **78**, 6432 (1995).

Table I: H_2 reaction rates [8]

Reaction	Expression	Threshold energy	Pre-exponential factor (m^3s^{-1})
Ionization	$e + H_2 \rightarrow e + H_2^+ + e$ $H_2^+ + H_2 \rightarrow H_3^+ + H$	15.4 eV 0 eV	1.0×10^{-14} H_3^+ is the dominant species
Excitation	$e + H_2 \rightarrow H_2^* + e$	12 eV	6.5×10^{-15}
Dissociation	$e + H_2 \rightarrow e + H + H$	10 eV	1.0×10^{-14}
Recombination	e + ion → neutral	0 eV	1.0×10^{-14}

Table II: Physical parameters for simulation

Run	Reactor pressure (Torr)	Absorbed power (W)	Plasma volume (cm^3)	Plasma radius (cm)	Plasma height (cm)
I	15	30	219.6	4.20	4.00
II	15	400	243.07	3.87	5.16
III	15	600	261.53	4	5.2
IV	15	900	297.78	4.15	5.5
V	25	400	110.08	2.97	3.97
VI	25	900	167.38	3.32	5.0
VII	40	400	80.32	2.68	3.56
VIII	40	900	66.73	2.44	3.61

Figure Captions

1. Schematic of the microwave plasma reactor used for diamond film deposition. The reactor has a 6 inch inner diameter.
2. Schematic of the grid used in the numerical solution of the electromagnetic and fluid plasma models.
3. (a) Radial electric field E_r (V/m) distribution in the entire reactor for a pressure of 15 Torr and absorbed microwave power of 30 W.
3. (b) Axial electric field E_z (V/m) distribution in the entire reactor for a pressure of 15 Torr and absorbed microwave power of 30 W.
4. (a) Radial electric field E_r (V/m) distribution in the entire reactor for a pressure of 15 Torr and absorbed microwave power of 900 W.
4. (b) Axial electric field E_z (V/m) distribution in the entire reactor for a pressure of 15 Torr and absorbed microwave power of 900 W.
5. (a) Radial electric field E_r (V/m) distribution in the plasma discharge region for a pressure of 15 Torr and absorbed microwave power of 30 W.
5. (b) Axial electric field E_z (V/m) distribution in the plasma discharge region for a pressure of 15 Torr and absorbed microwave power of 30 W.
6. (a) Radial electric field E_r (V/m) distribution in the plasma discharge region for a pressure of 15 Torr and absorbed microwave power of 900 W.
6. (b) Axial electric E_z (V/m) field distribution in the plasma discharge region for a pressure of 15 Torr and absorbed microwave power of 900 W.
7. (a) Absorbed microwave power distribution in the plasma discharge for a pressure of 15 Torr and absorbed microwave power of 30 W.

7. (b) Absorbed microwave power distribution in the plasma discharge for a pressure of 15 Torr and absorbed microwave power of 900 W.
8. (a) Electron temperature (K) distribution for a pressure of 15 Torr and absorbed microwave power of 30 W.
8. (b) Electron temperature (K) distribution for a pressure of 15 Torr and absorbed microwave power of 900 W.
9. (a) Electron density distribution for a pressure of 15 Torr and absorbed microwave power of 30 W.
9. (b) Electron density distribution for a pressure of 15 Torr and absorbed microwave power of 900 W.
10. H_2 dissociation rate ($m^{-3}s^{-1}$) in the plasma discharge for a pressure of 15 Torr and absorbed microwave power of 400 W.
11. (a) Average electron temperature versus absorbed plasma power for three different reactor pressures of 15, 25, and 40 Torr.
11. (b) Maximum calculated electron temperature versus absorbed plasma power for three different reactor pressures of 15, 25, and 40 Torr.
12. (a) Average electron density versus absorbed plasma power for three different reactor pressures of 15, 25 and 40 Torr.
12. (b) Maximum computed electron density versus absorbed plasma power for three reactor pressures of 15, 25, and 40 Torr.

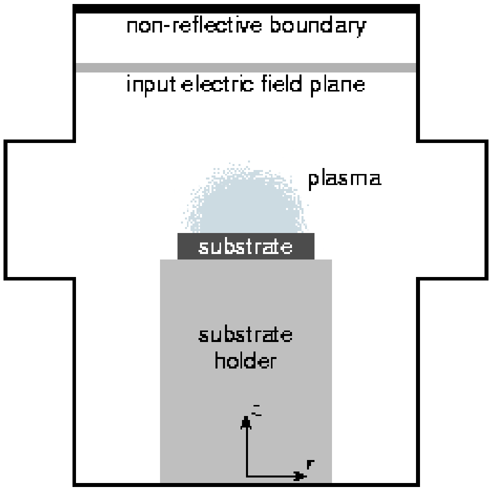
non-reflective boundary
input electric field plane
plasma
substrate
substrate holder
z
r

Figure 1

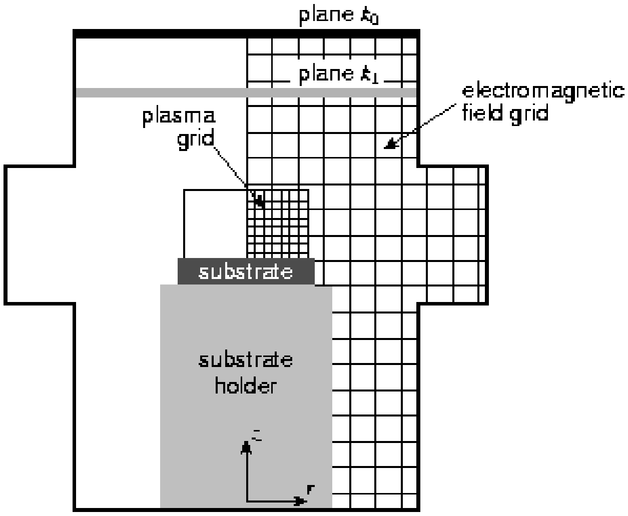
plane k_0
plane k_1
electromagnetic field grid
plasma grid
substrate
substrate holder
z
r

Figure 2

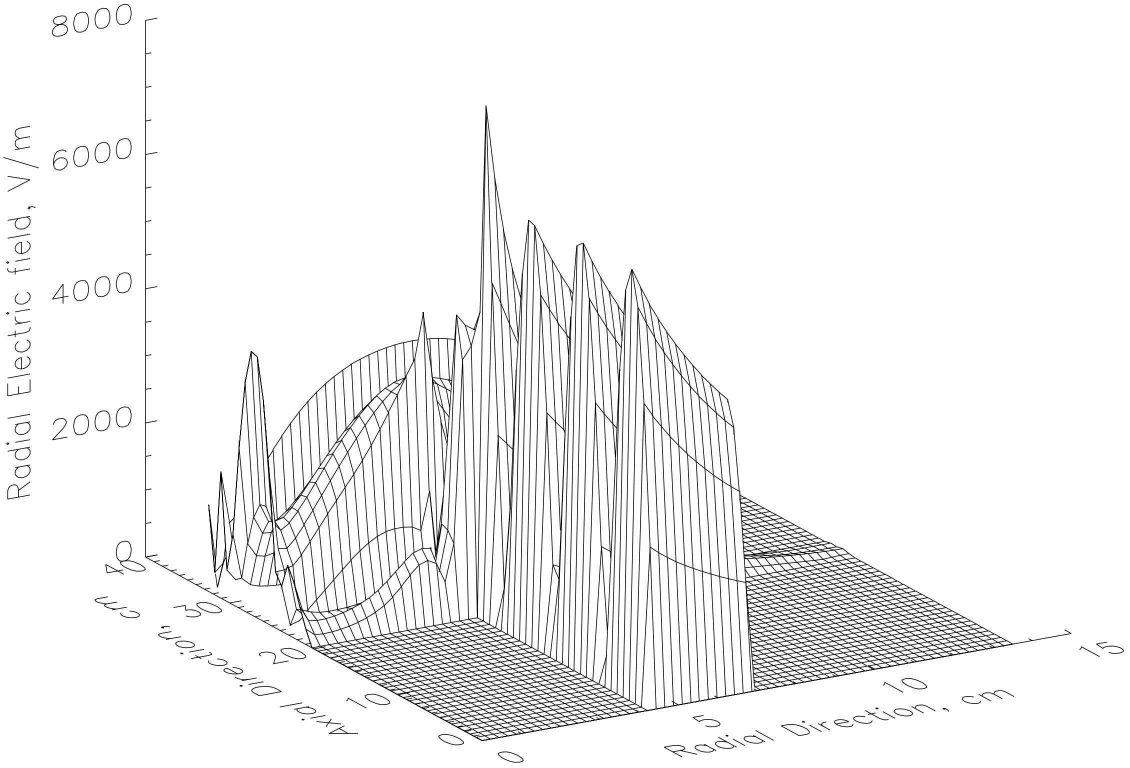

8000
6000
4000
2000
0
Radial Electric field, V/m
40
30
20
10
0
Axial Direction, cm
0
5
10
15
Radial Direction, cm

Figure 3a

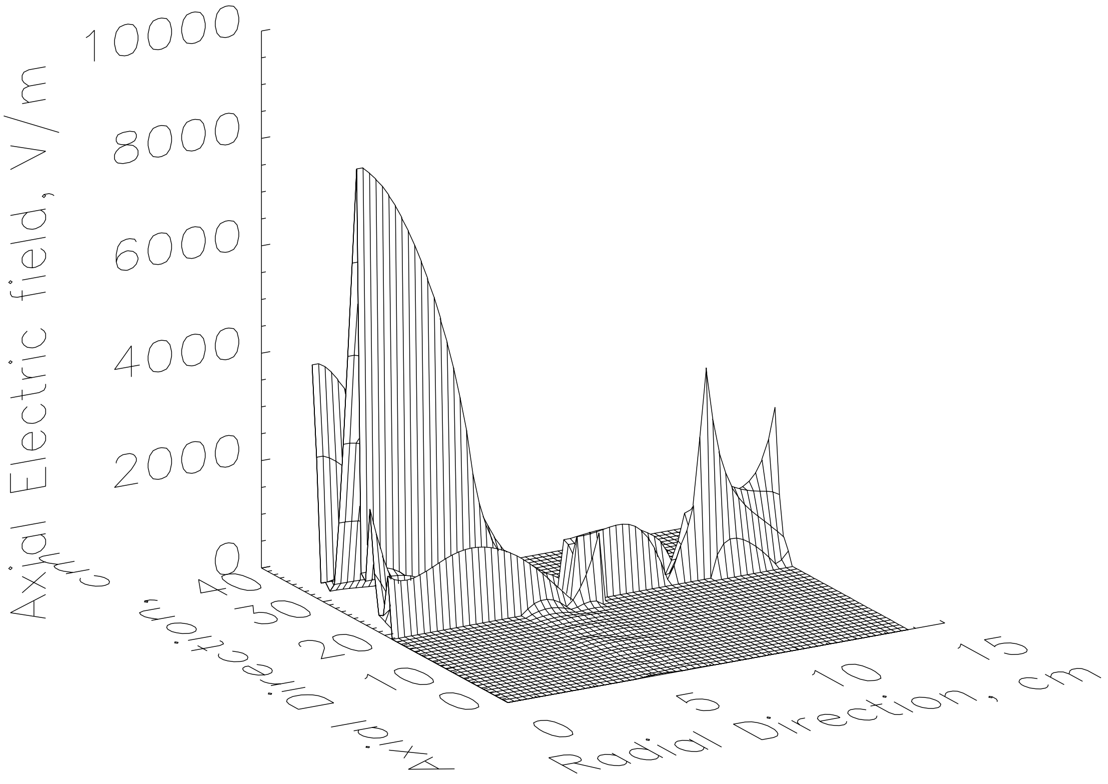
10000
8000
6000
4000
2000
0
Axial Electric field, V/m
40
30
20
10
0
Axial Direction, cm
0
5
10
15
Radial Direction, cm

Figure 3b

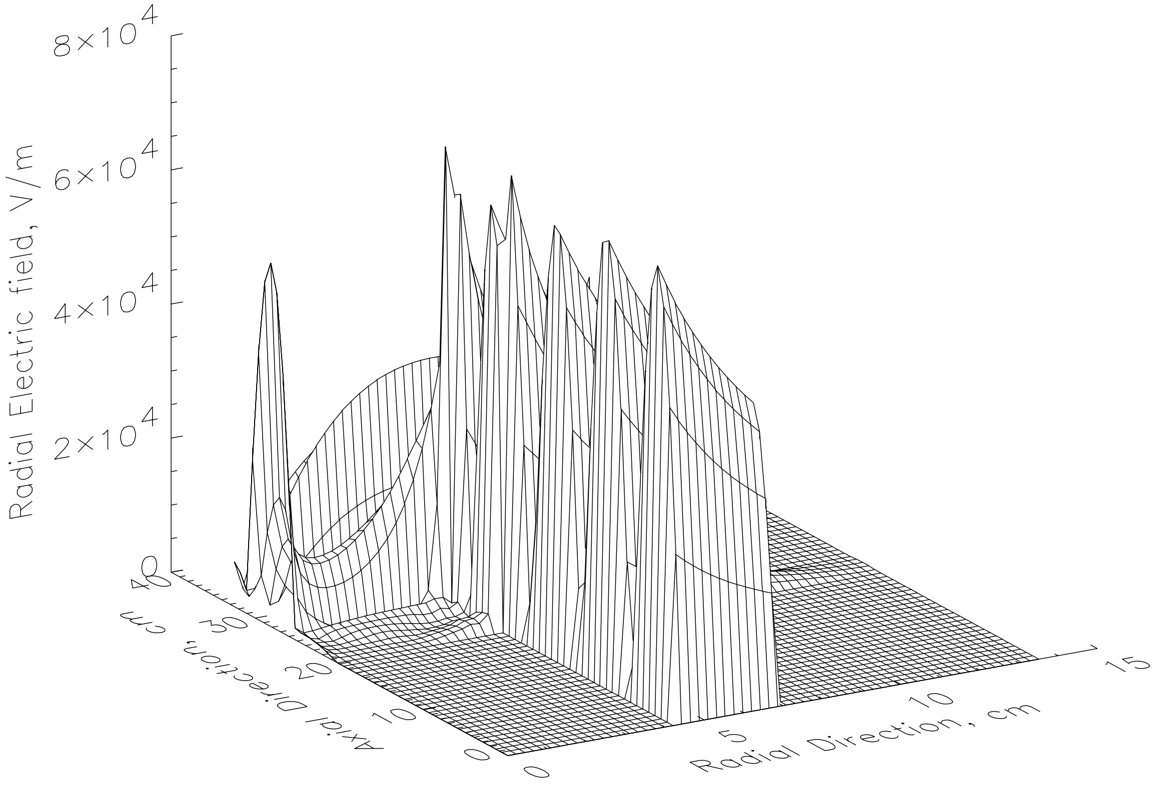
8×10^4
6×10^4
4×10^4
2×10^4
0
Radial Electric field, V/m
40
30
20
10
0
Axial Direction, cm
0
5
10
15
Radial Direction, cm

Figure 4a

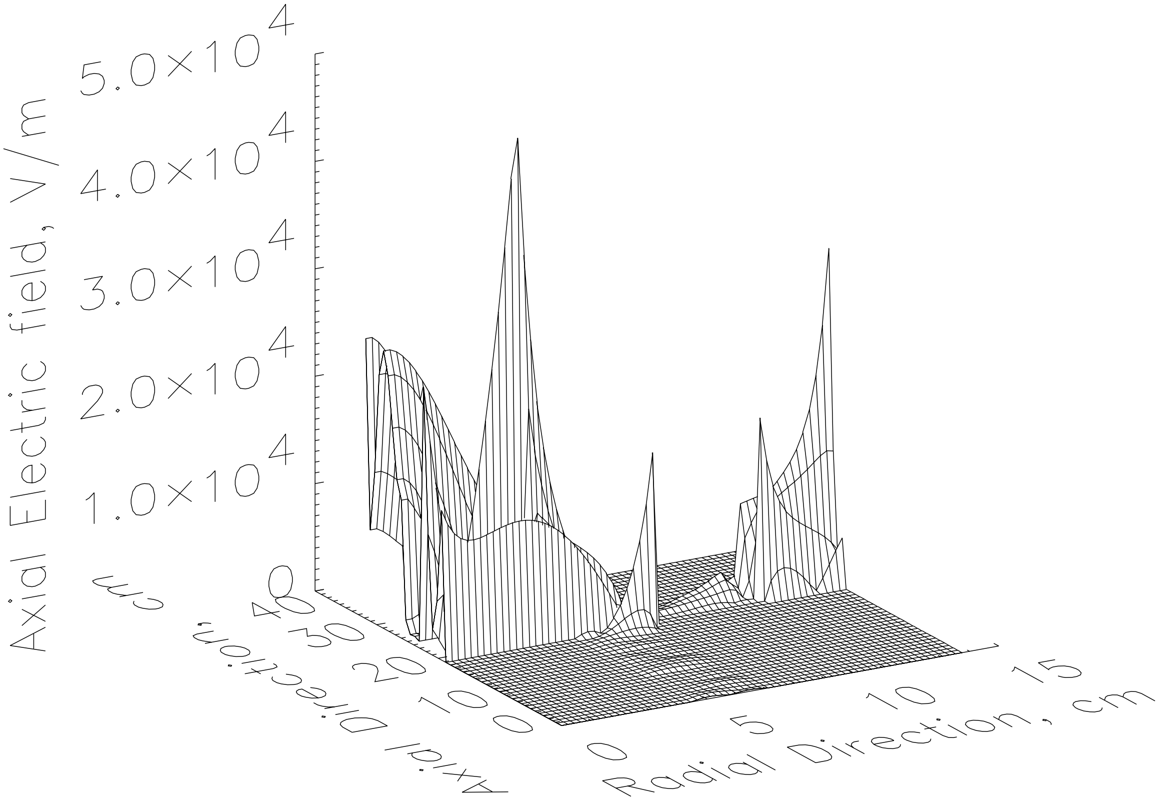
Axial Electric field, V/m
0
1.0×10^4
2.0×10^4
3.0×10^4
4.0×10^4
5.0×10^4
Axial Direction, cm
0
10
20
30
40
Radial Direction, cm
0
5
10
15

Figure 4b

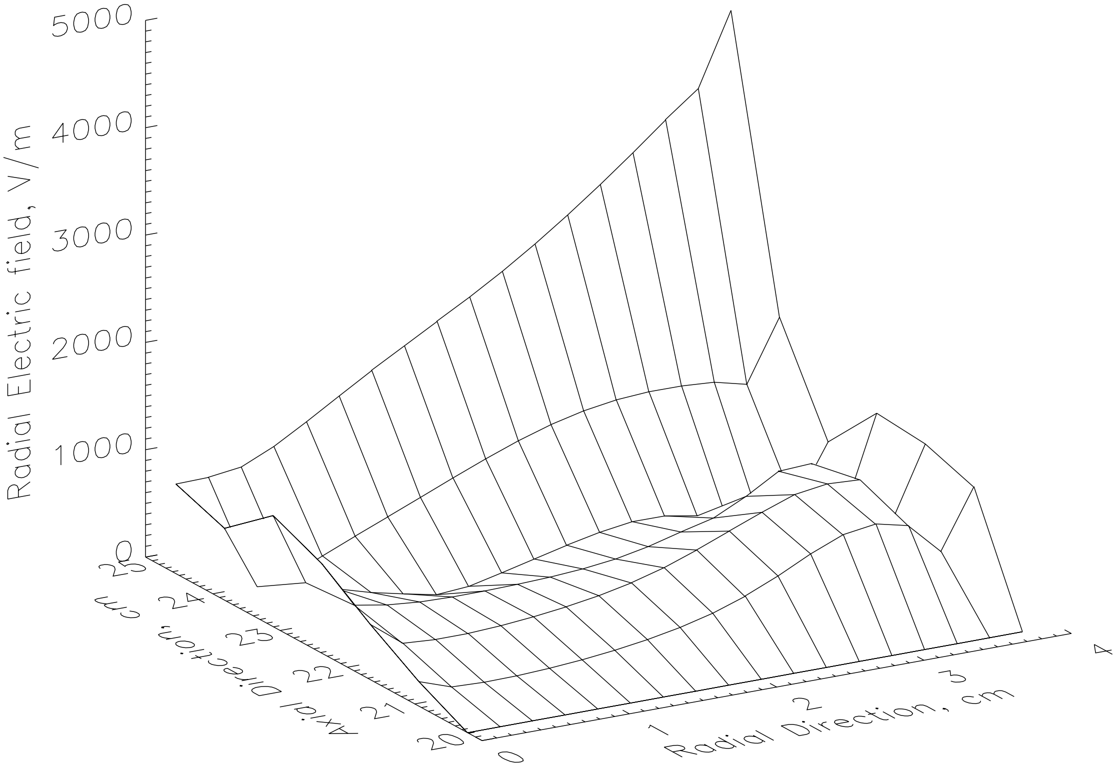
Radial Electric field, V/m
5000
4000
3000
2000
1000
0
Axial Direction, cm
25
24
23
22
21
20
Radial Direction, cm
0
1
2
3
4

Figure 5a

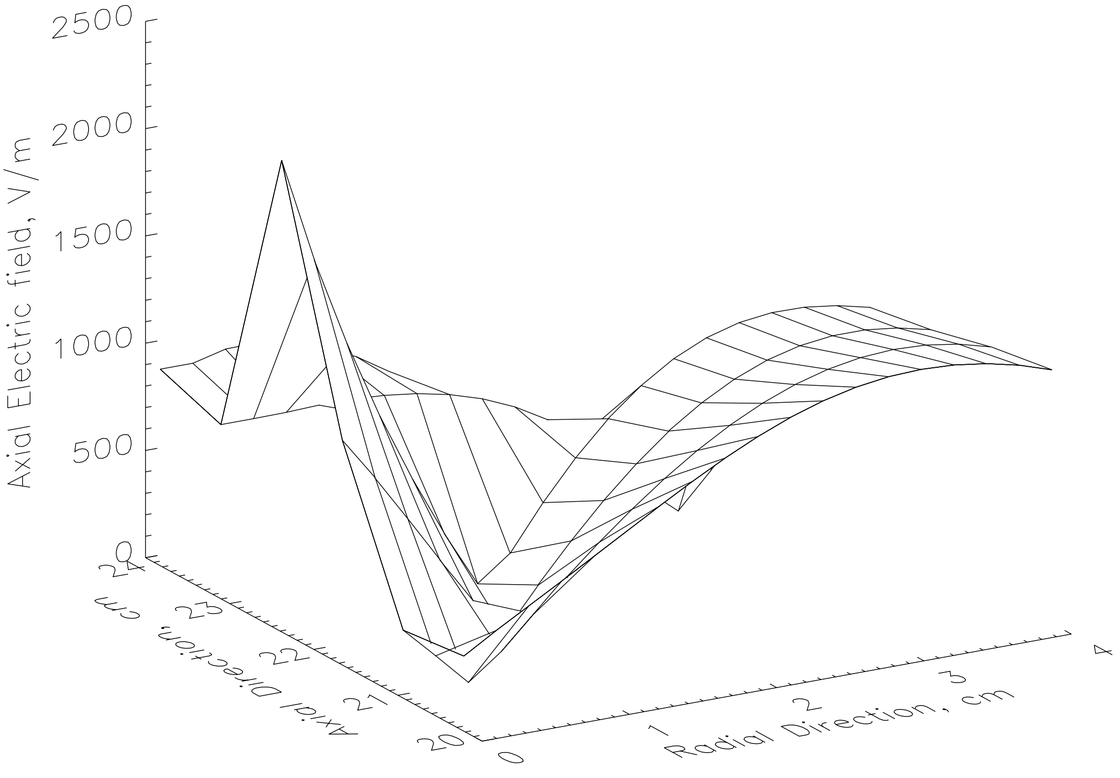
2500
2000
1500
1000
500
0
Axial Electric field, V/m
24
23
22
21
20
Axial Direction, cm
0
1
2
3
4
Radial Direction, cm

Figure 5b

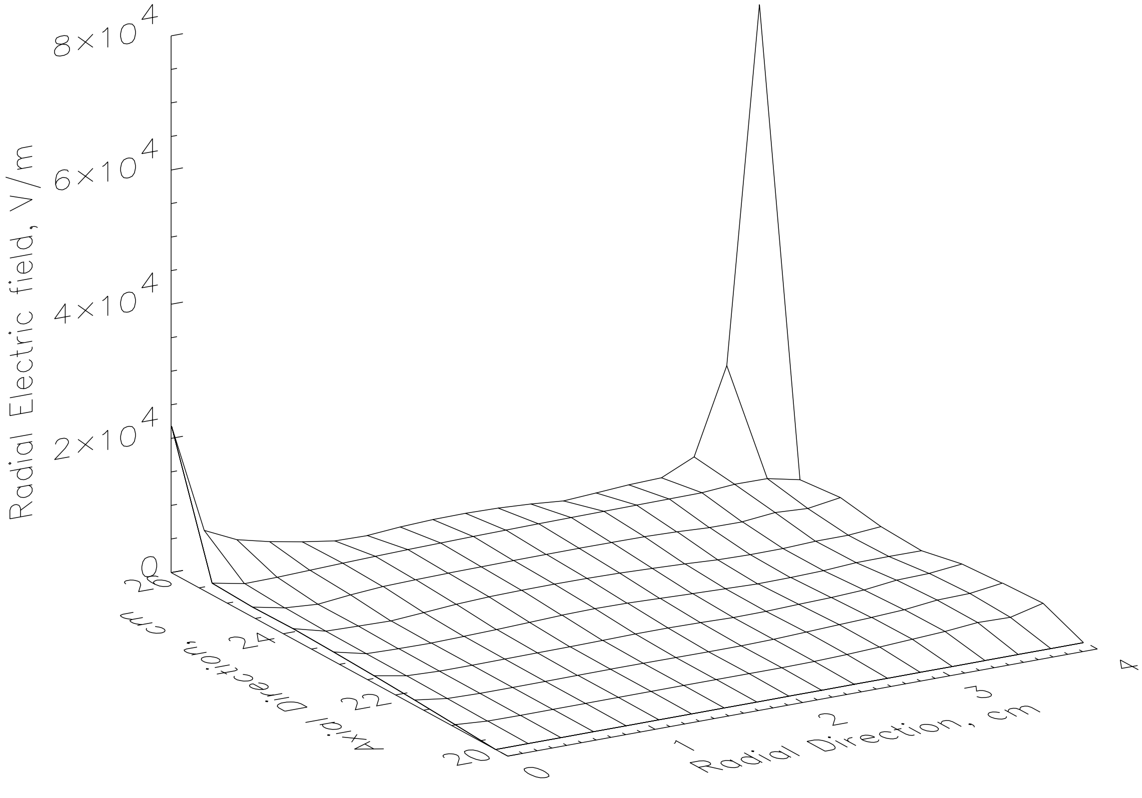
8×10^4
6×10^4
4×10^4
2×10^4
0
Radial Electric field, V/m
20
22
24
26
Axial Direction, cm
0
1
2
3
4
Radial Direction, cm

Figure 6a

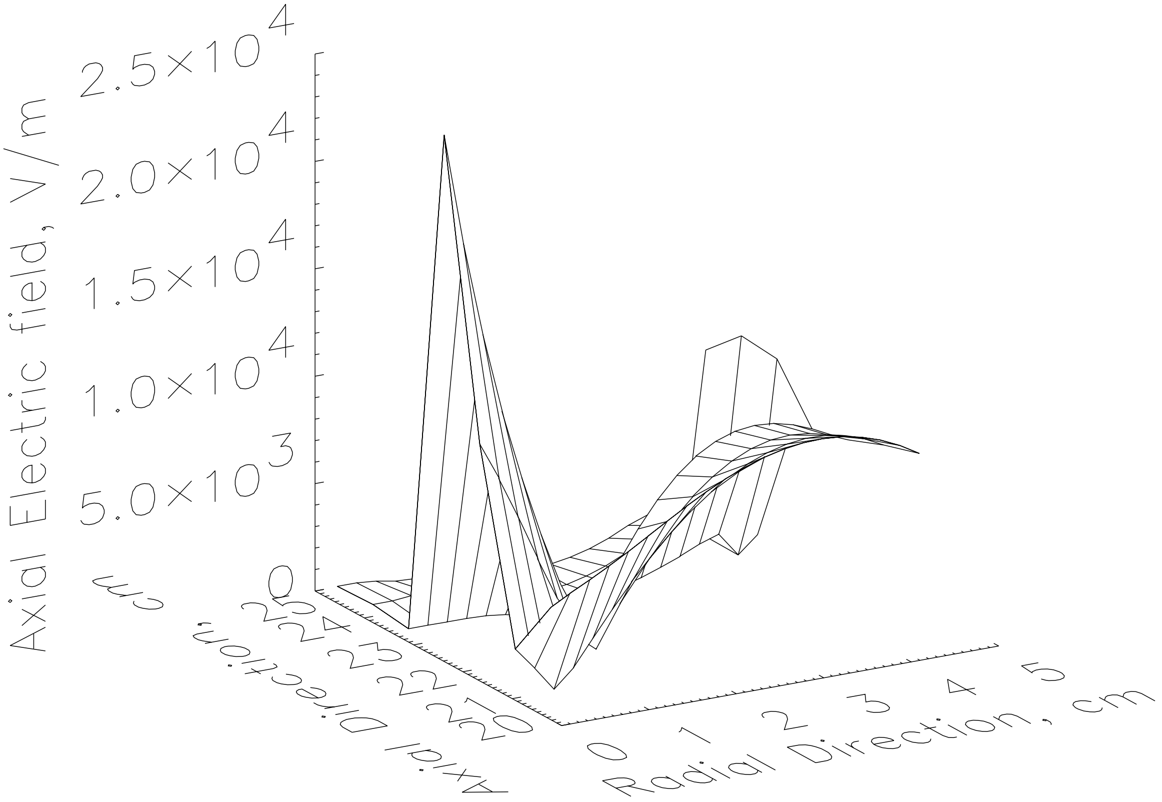
Axial Electric field, V/m
2.5×10^4
2.0×10^4
1.5×10^4
1.0×10^4
5.0×10^3
0
Axial Direction, cm
25
24
23
22
21
20
Radial Direction, cm
0
1
2
3
4
5

Figure 6b

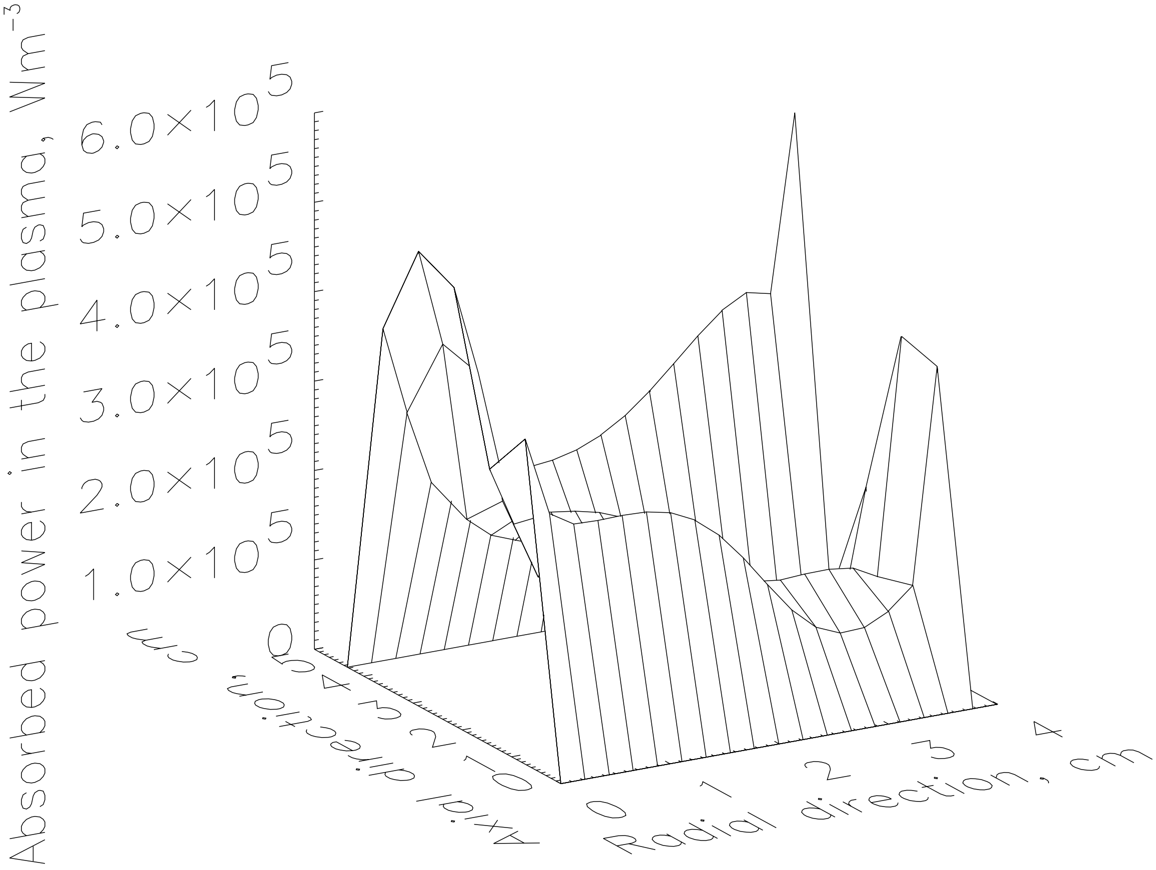
Absorbed power in the plasma, Wm^{-3}
0
1.0×10^5
2.0×10^5
3.0×10^5
4.0×10^5
5.0×10^5
6.0×10^5
Axial direction, cm
0
1
2
3
4
Radial direction, cm
0
1
2
3
4

Figure 7a

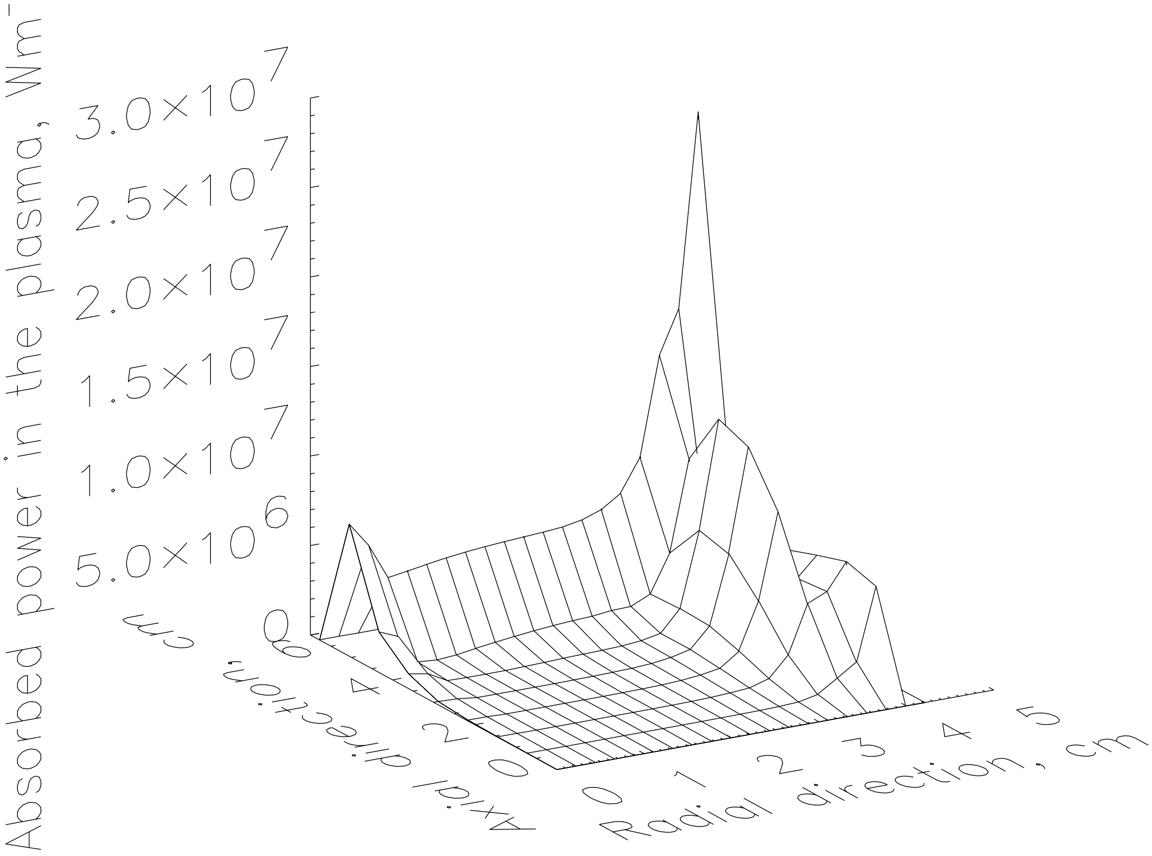
Absorbed power in the plasma, Wm^{-3}
0
5.0×10^6
1.0×10^7
1.5×10^7
2.0×10^7
2.5×10^7
3.0×10^7
Axial direction, cm
0
2
4
6
Radial direction, cm
0
1
2
3
4
5

Figure 7b

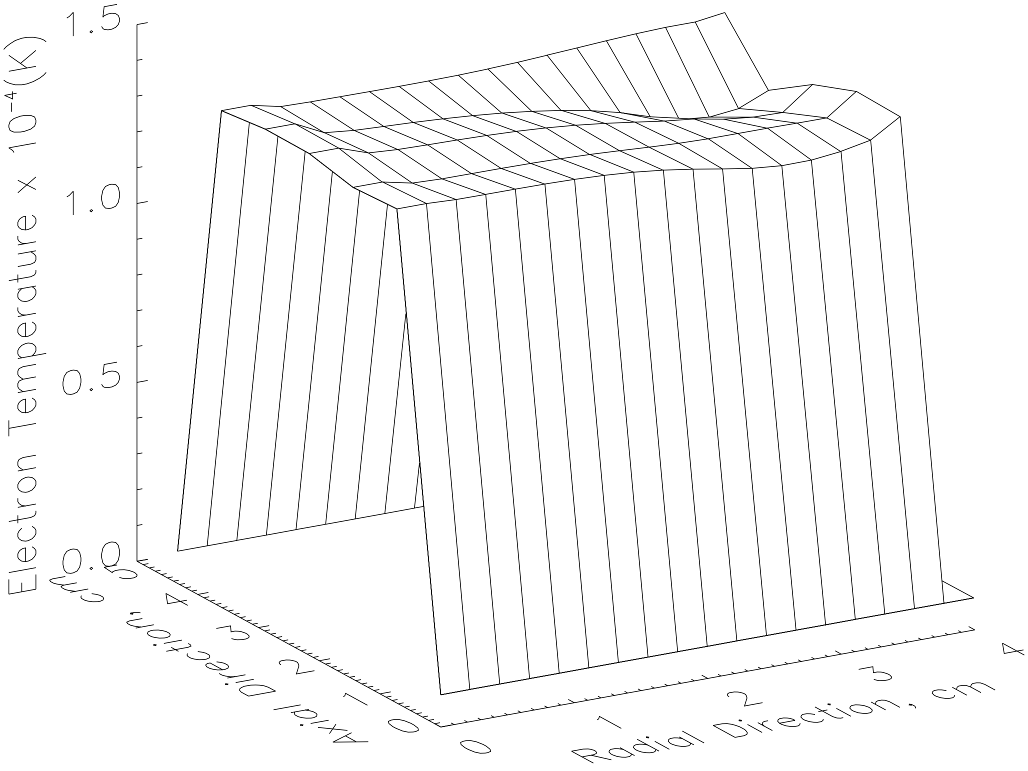
Electron Temperature x 10⁻⁴(K)
0.0
0.5
1.0
1.5
Axial Direction, cm
0
1
2
3
4
5
Radial Direction, cm
0
1
2
3
4

Figure 8a

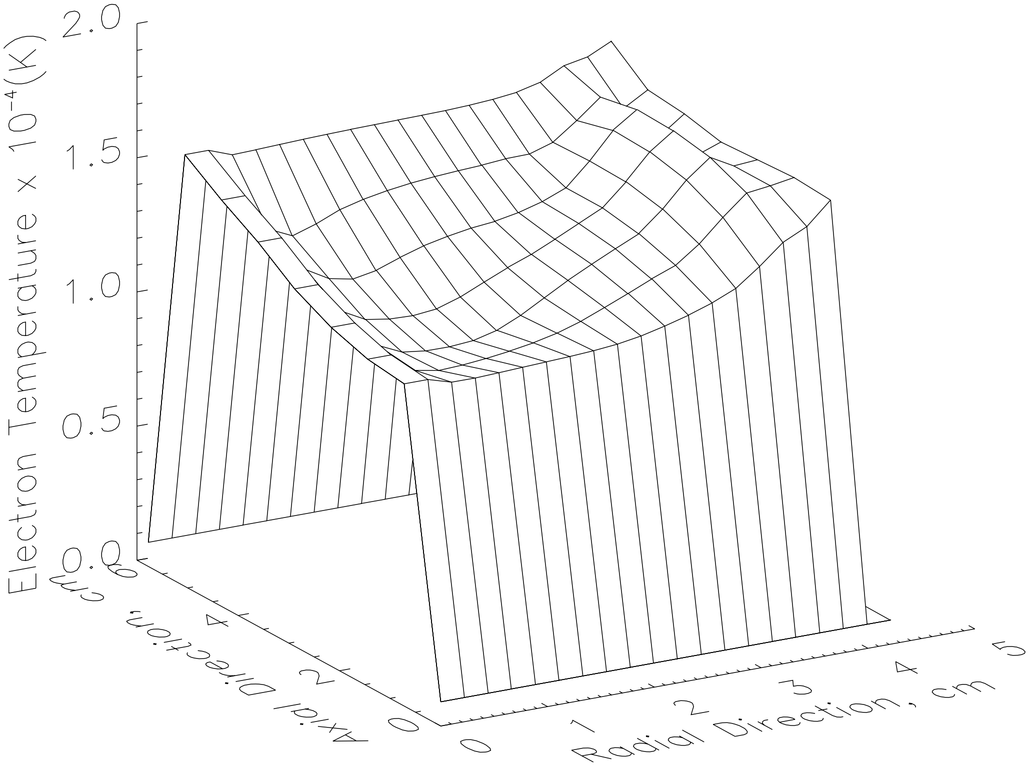
Electron Temperature x 10⁻⁴(K)
0.0
0.5
1.0
1.5
2.0
Axial Direction, cm
0
2
4
6
Radial Direction, cm
0
1
2
3
4
5

Figure 8b

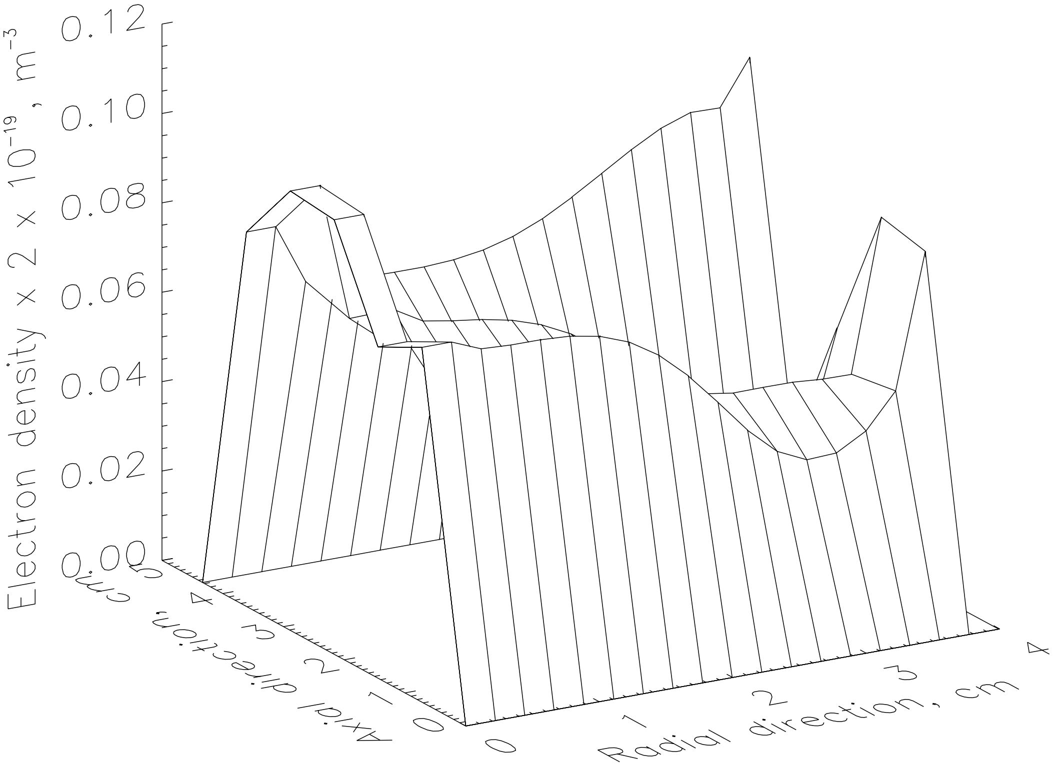
Electron density x 2 x 10^{-19}, m^{-3}
0.00
0.02
0.04
0.06
0.08
0.10
0.12
Axial direction, cm
0
1
2
3
4
5
Radial direction, cm
0
1
2
3
4

Figure 9a

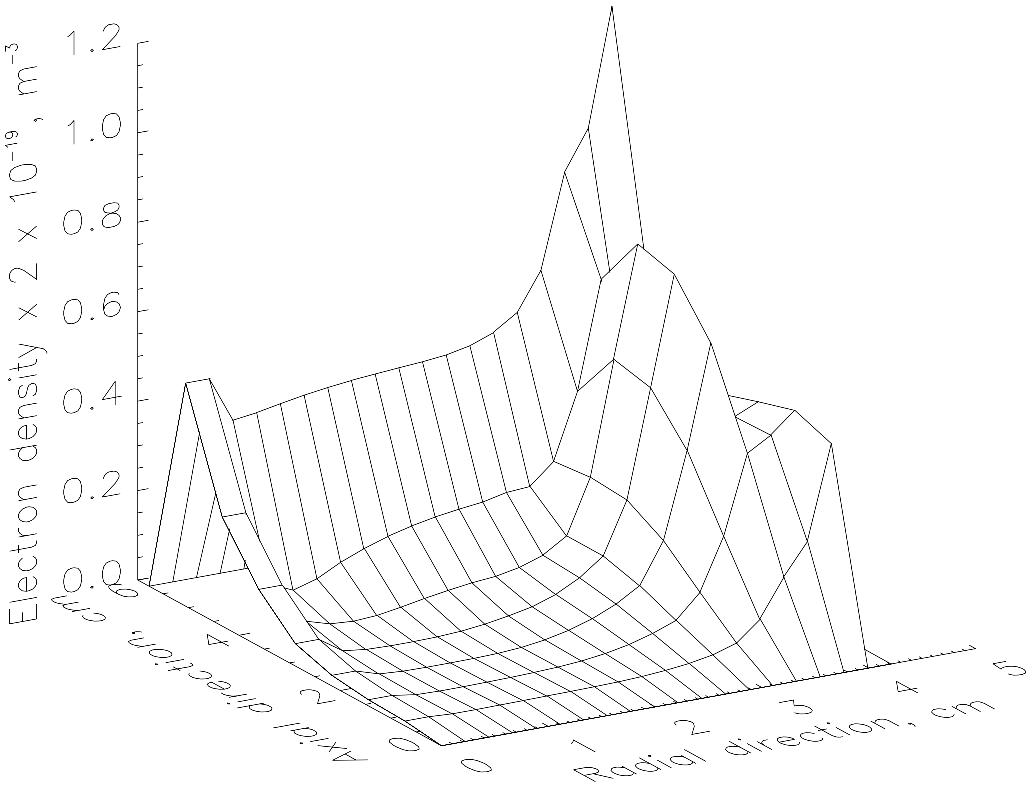
Electron density × 2 × 10^{-19}, m^{-3}
0.0
0.2
0.4
0.6
0.8
1.0
1.2
Axial direction, cm
0
2
4
6
Radial direction, cm
0
1
2
3
4
5

Figure 9b

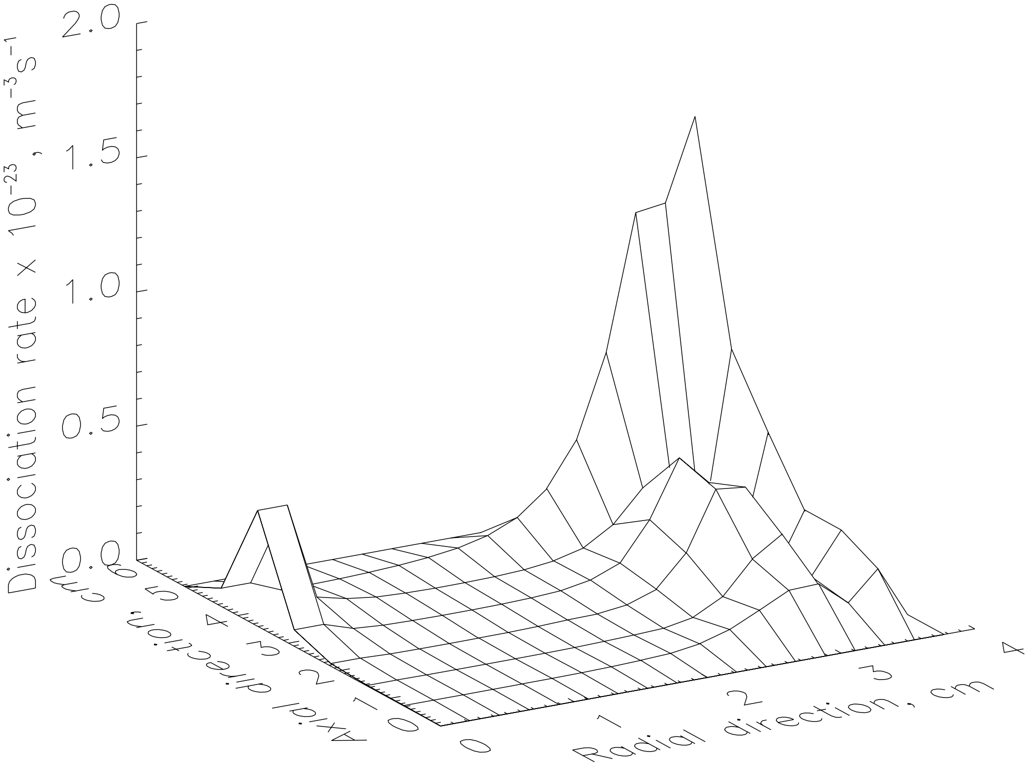
Dissociation rate x 10^{-23}, $m^{-3}s^{-1}$
0.0
0.5
1.0
1.5
2.0
Axial direction, cm
0
1
2
3
4
5
6
Radial direction, cm
0
1
2
3
4

Figure 10

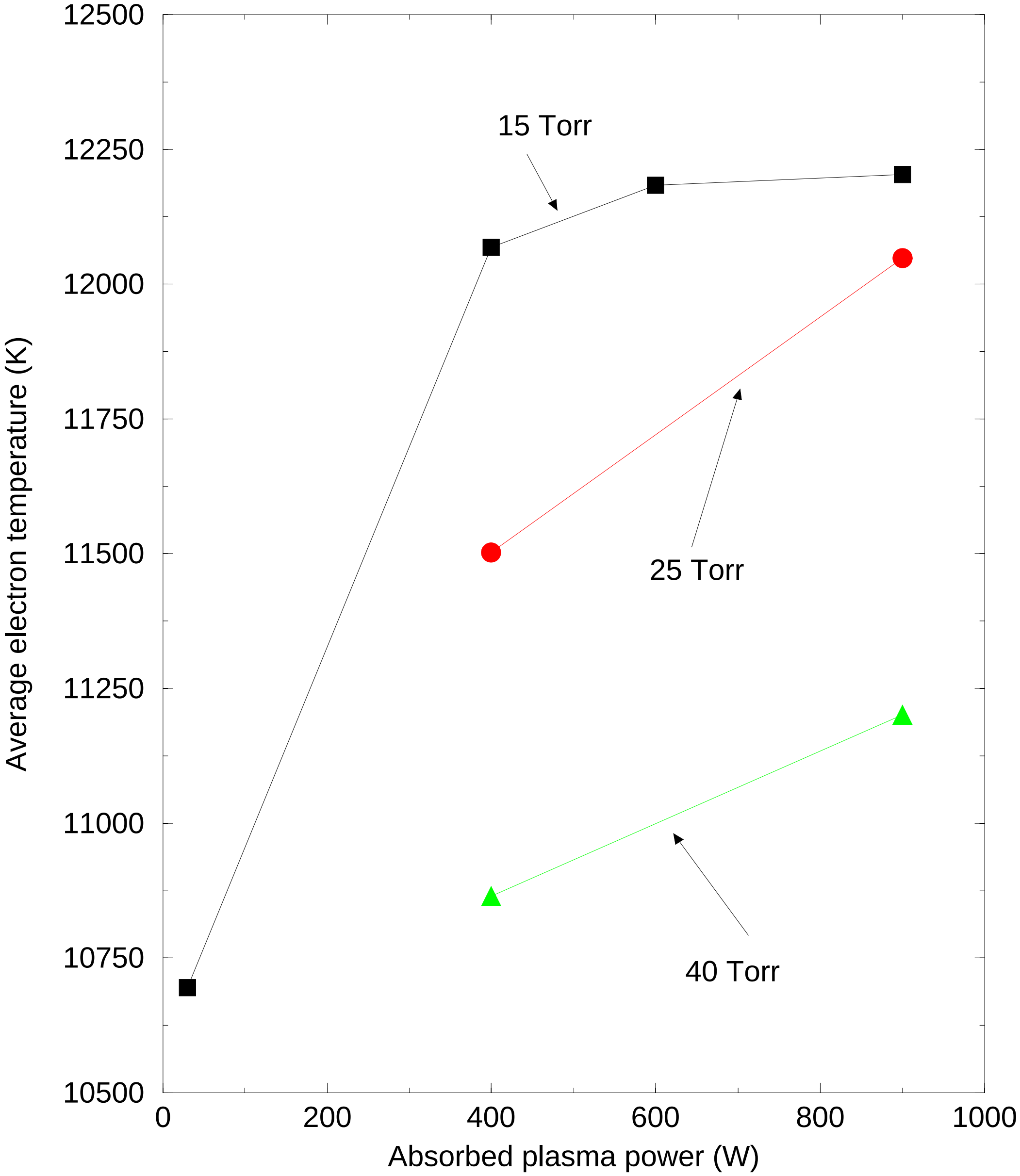

12500
12250
12000
11750
11500
11250
11000
10750
10500
Average electron temperature (K)
0
200
400
600
800
1000
Absorbed plasma power (W)
15 Torr
25 Torr
40 Torr

Figure 11a

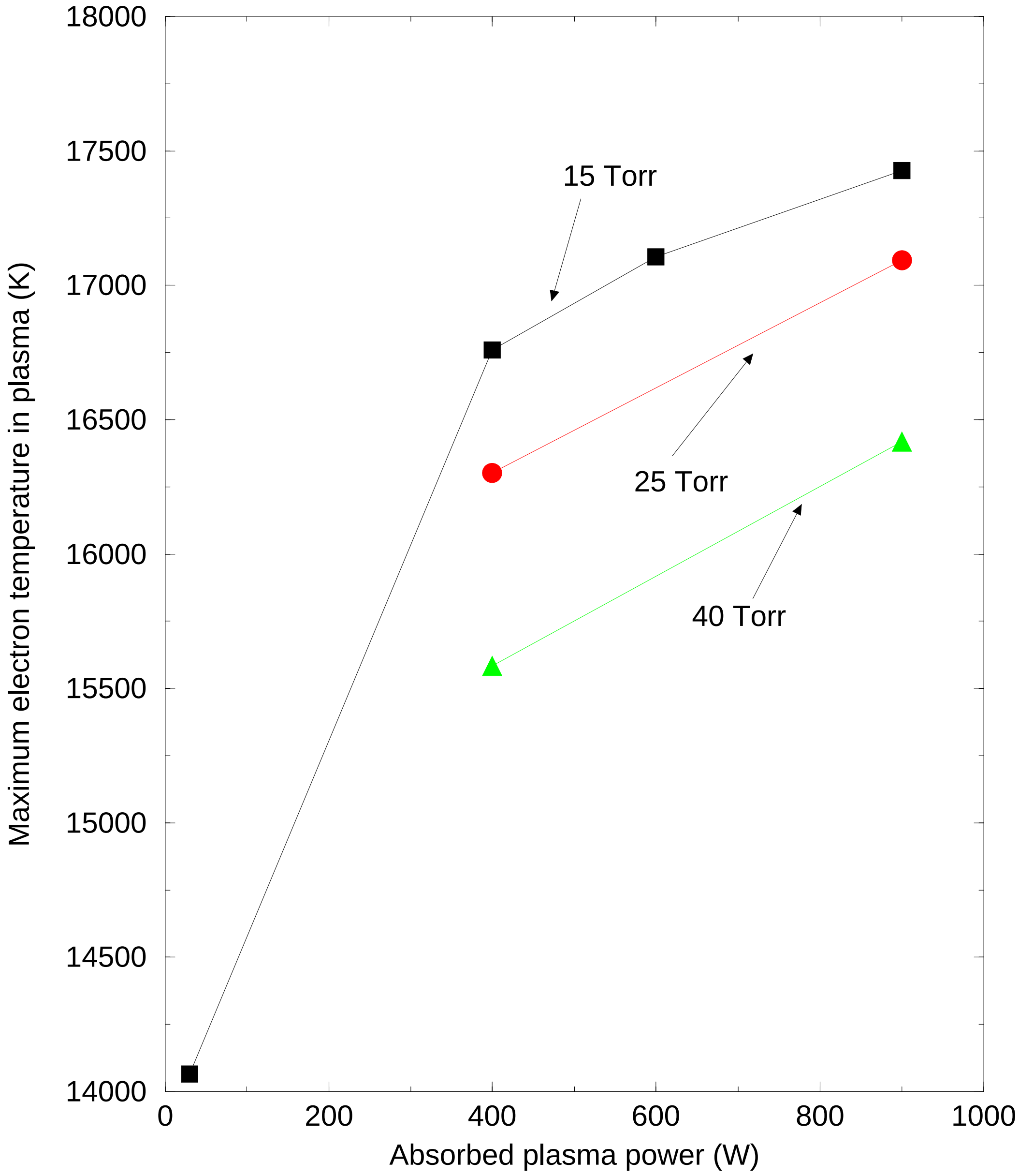

18000
17500
17000
16500
16000
15500
15000
14500
14000
0
200
400
600
800
1000
Absorbed plasma power (W)
Maximum electron temperature in plasma (K)
15 Torr
25 Torr
40 Torr

Figure 11b

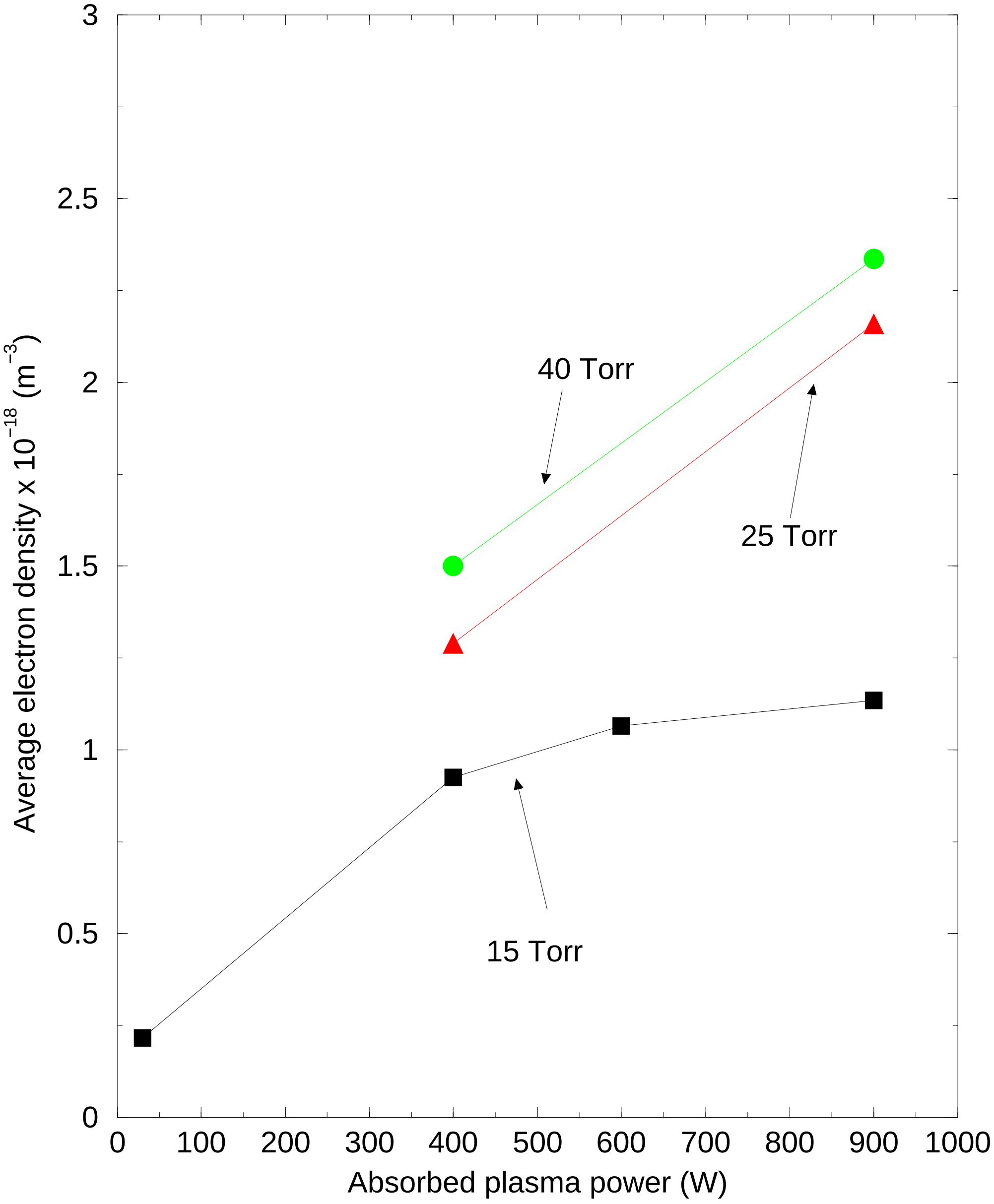
Average electron density x 10^{-18} (m^{-3})
0
0.5
1
1.5
2
2.5
3
0
100
200
300
400
500
600
700
800
900
1000
Absorbed plasma power (W)
40 Torr
25 Torr
15 Torr

Figure 12a

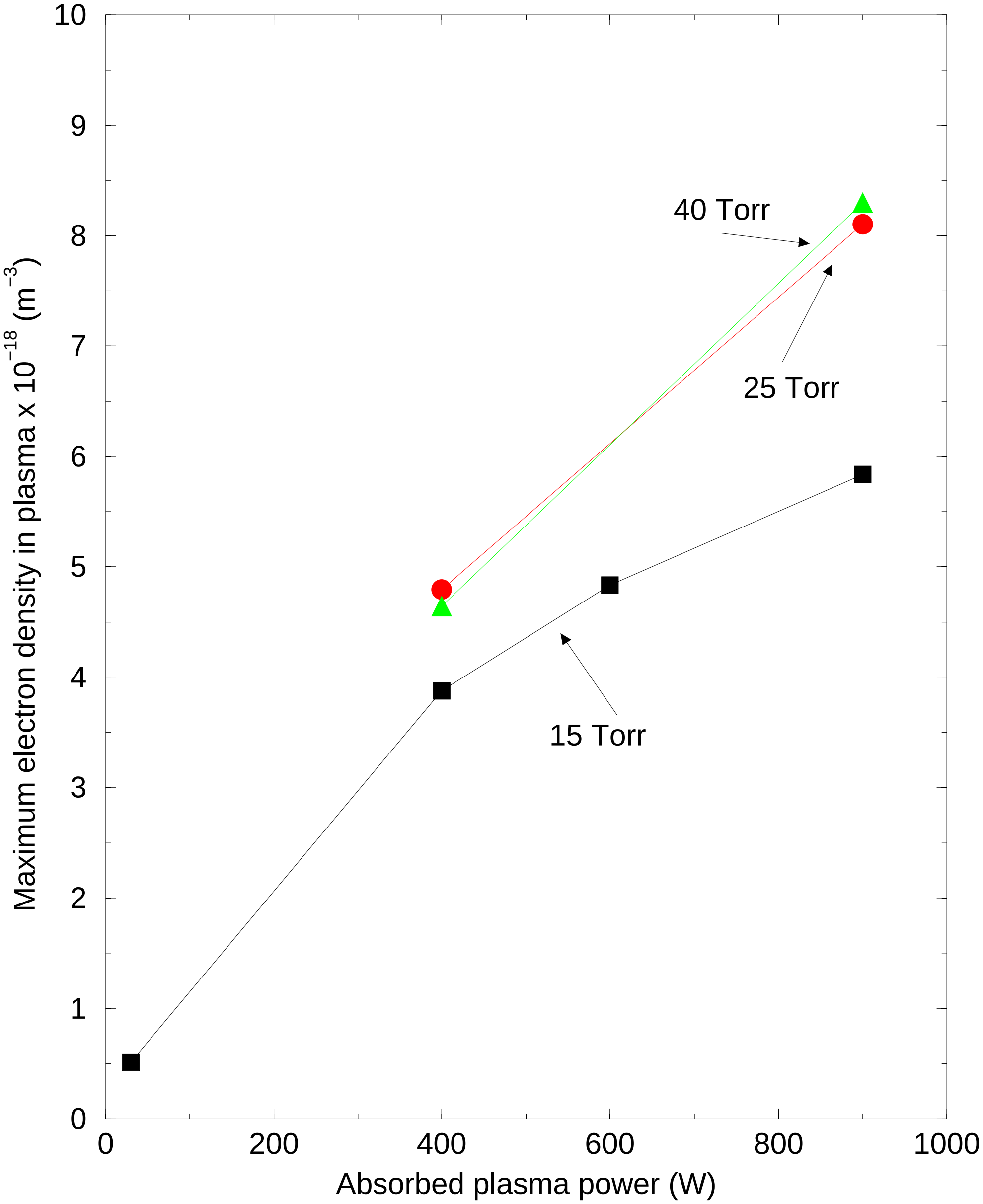
Maximum electron density in plasma x 10^{-18} (m^{-3})
Absorbed plasma power (W)
0
1
2
3
4
5
6
7
8
9
10
0
200
400
600
800
1000
40 Torr
25 Torr
15 Torr

Figure 12b